Collective dynamics of two-dimensional swimming bacteria: Experiments and models

Gil Ariel,[1] Marina Sidortsov,[2] Shawn D. Ryan,[3] Sebastian Heidenreich,[4] Markus Bär,[4] and Avraham Be'er[2,5,*]

[1]*Department of Mathematics, Bar-Ilan University, Ramat Gan 52000, Israel*

[2]*Zuckerberg Institute for Water Research, The Jacob Blaustein Institutes for Desert Research, Ben-Gurion University of the Negev, Sede Boqer Campus 84990, Midreshet Ben-Gurion, Israel*

[3]*Department of Mathematics, Cleveland State University, Cleveland, Ohio 44115, USA*

[4]*Department of Mathematical Modelling and Data Analysis, Physikalisch-Technische Bundesanstalt Braunschweig und Berlin, Abbestrasse 2-12, D-10587 Berlin, Germany*

[5]*Department of Physics, Ben-Gurion University of the Negev, Beer Sheva 84105, Israel*

(Received 14 June 2018; published 24 September 2018)

The physical properties of collectively swimming bacteria have been thoroughly investigated both experimentally and theoretically using simulations. While models successfully predict some aspects of the dynamics observed in experiments, both models and experiments vary in their underlying assumptions and physical conditions. Hence, it is not clear which models are appropriate for which experimental setups. Here, we study, both experimentally and using two types of models (agent-based and continuous), the statistics of two strains of *Serratia marcescens*, wild-type and a nontumbling strain, swimming on a two-dimensional monolayer at varying concentrations. The experimental setup allows for a direct comparison with simulation results. Both models capture some aspects of the dynamics but fail at displaying others, especially at high densities. In particular, the effect of tumbling is much more significant than mere rotational (angular) diffusion.

DOI: 10.1103/PhysRevE.98.032415

I. INTRODUCTION

Motile bacteria are considered as self-propelled particles because their rotating flagella create a thrust that pushes them forward in viscous environments. At low cell densities, bacteria exhibit a movement pattern called "run and tumble," characterized by straight trajectories (runs) interspersed by shorter, random reorientation events (tumbles) [1]. The chemotaxis signaling network operates in controlling the frequency of tumbles, enabling an average bias toward or away from desired regions in the medium [2]. Nontumbling, i.e., smooth-swimmer (SS), strains move in straight lines, or weakly curved trajectories if close to surfaces, and are unable to navigate. At high cell densities, such as in crowded bulk cultures or in relatively thick swarm colonies, interactions between the individuals become dominant [3–61]. These include cell-cell steric (contact) interactions that are more dominant in rod-shaped cells [3–9], and hydrodynamic interactions between the cells and the fluid in which they move [10–14,62–66]. Such interactions lead to a collective flow of the cells with dynamic whirls and jets composed of thousands of individuals. Such collective motion of cells has been named as mesoscale turbulence, active turbulence, or bacterial turbulence, due to its phenomenological similarity with hydrodynamical turbulence at high Reynolds numbers; see, e.g., [5,15]. In recent theory, simple models for these have been proposed and analyzed [16–19]. Related phenomena were also found in experimental studies of other systems like active colloids [20] and tissues [11]. In some situations, e.g., during swarming, it is known that chemotaxis is suppressed during high-density collective motion [21]. This implies that tumbling events are uncoupled from the chemotaxis signaling network and smooth-swimmers should form patterns similar to those obtained for the wild-type (WT). In a recent work on swarming bacteria [21], it was shown that tumbling (and not chemotaxis) is responsible for some specific characteristics of the swarm. For this reason, the exact role of flagellar tumbling in forming collective motion is unclear.

Collective bacterial motion has also been observed in cells that are confined to move within thin, two-dimensional (2D) films. These include swimming bacteria that inhabit a single layer or a film, or 2D swarm colonies where the cells spread ahead in a monolayer and do not form stacked layers (e.g., [12,22–26]). In this work, we study experimentally and theoretically the role of tumbling (rotational diffusion) in collective motion of bacteria *swimming in a monolayer*, by gradually changing their density from sparsely moving cells to densely packed ones. Therefore, these experiments are more appropriate for comparison with theoretical predictions than previous experiments with multilayer swarms (e.g., [3,21,27–37]), in which the density could not be controlled.

Here, we compare the experimental collective statistics of the bacterial flow [Figs. 1(a) and 1(b)] with two previously studied models of collective bacterial motion, adapted to the system studied here—one discrete or agent-based [Figs. 1(c) and 1(d)], and one continuous [Figs. 1(e) and 1(f)]. In the discrete approach, the characteristics of individuals (or groups) are described, for example, the rules for interactions between single agents or their environment. Agent-based simulations offer a simple, yet versatile, method for modeling complicated many-particle systems (e.g., [37]). In contrast, continuous

*beera@bgu.ac.il

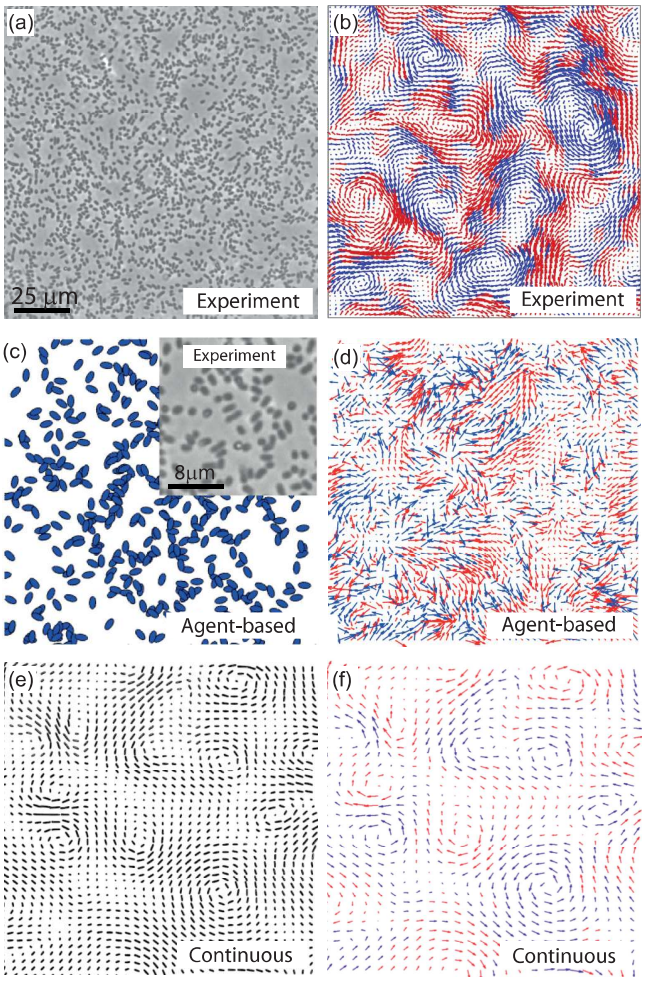

FIG. 1. Collective swimming of wild-type *S. marcescens*; experimental observations. (a) A microscopic phase-contrast image and (b) the velocity field obtained using optical flow analysis. Red and blue arrows indicate clockwise and counterclockwise rotation, respectively. (c) A snapshot from the agent-based simulation and (d) the velocity field of the flow. The inset shows an image from experiments at a similar magnification. (e) A snapshot of the polarization and (f) velocity fields in the continuous model.

models describe characteristics shared by many cells, for example, local density averages, polar or nematic alignment, etc. Such coarse-grained descriptions have been proposed for different active systems ranging from flying birds and schools of fish to moving bacteria or artificial microswimmers (see Marchetti *et al.* [62] for a recent review, and [67]).

In [14,35,38], Ryan *et al.* have studied an agent-based model in which the motion of each cell is determined by its self-propulsion, hydrodynamic interaction with the local fluid flow, and near-field excluded-volume interactions. Each bacterium is modeled as a point dipole in a Stokes flow and a soft repulsive potential. Particles are advected and rotated by the local flow generated by other cells around it. The point dipole approach is computationally efficient for simulating a wide range of experimentally observable densities. Nonetheless, some model assumptions (for example, the soft-core repulsion and additivity of the flow generated by cells) may not be valid at very high densities. Here, we adapt the point dipole model successfully used in [35] to describe the bacterial dynamics in thin films. A detailed formulation of the model is given in Sec. II D.

In [39], Dunkel *et al.* proposed a phenomenological theory to model the collective motion of dense bacterial suspensions. The model involves derivatives up to the fourth order of an effective coarse-grained velocity field. The main motivation was to reproduce the experimental phenomenology reported by Wensink *et al.* [5], which was achieved by combining characteristic features of the Swift-Hohenberg equation with the Toner-Tu approach. In some dynamical states found experimentally [21,35,40], it is necessary to distinguish between orientation and the hydrodynamic flow of the suspension. Recently, the phenomenological model [39] was extended and derived from a microscopic model, similar to the agent-based approach described above, that captures the hydrodynamic flow and the orientational dynamics of cells [64,65]. Recently, extended fourth order model equations have been derived from the microscopic dynamics of hydrodynamically interacting swimmers with short-range polar alignment in 2D [64] and with short-range polar and nematic alignment in 2D and three dimensions (3D) [65]. The continuum theory was derived by coarse-graining the microscopic model. A key assumption to this approach was that the bacterial concentration of the suspension is constant and density fluctuations can be neglected. Here, we use a variant continuum equation from [68] in which the collective dynamics of bacteria with polar alignment are confined to a quasi-2D film. In addition, steric interactions are not directly considered, but alignment interactions are included. A detailed formulation of the model is given in Sec. II E.

Computer simulations and models often describe tumbling as an effective angular diffusion, which phenomenologically takes into account any form of noise in the cell direction. These include thermal fluctuations, random turns due to hydrodynamic interactions with fluctuating flows, and tumbling (flagellar rotor switching). By varying the angular diffusion coefficient, one can study the effective contribution of tumbling on the collective motion at varying bacterial concentrations. Overall, the comparison between experiments and simulation shows that, while models successfully capture some of the essential features of the bacterial dynamics at low to moderate concentrations, they fail at high surface fractions. Moreover, we show that the role of flagellar motor switching goes beyond simple effective diffusion.

II. MATERIALS AND METHODS

A. Bacterial strains and growth protocol

Experiments were performed with *Serratia marcescens* 274, which is a gram-negative flagellated species, used as a model system in many previous quantitative experiments [12,22,26,34]. During exponential growth (density $\sim 10^7$ cells/ml) the cells are rod shaped (aspect ratio ~ 3) but in overnight cultures they reach a much higher density (2×10^9 cells/ml) and the cells shrink to a nearly spherical shape (average aspect ratio of about 1.5) possibly due to starvation. Individual wild-type (WT) cells swimming within

sparse suspensions control the frequency of rotor switching between states of runs and tumbles, depending on the chemotactic sensing system. Chemotactic signal transduction and the corresponding motor output enable the cells to navigate toward (or away from) chemical gradients in the medium. In sparse situations, the WT cells exhibit run durations that last 1.8 ± 0.6 s with tumbling durations of 0.2 ± 0.07 s. By contrast, the nontumbling mutants (Sm1420) are smooth-swimmers (SS) that do not exhibit flagellar rotor switching because the flagellar rotor is nearly exclusively biased in the counterclockwise direction. As a result, cells experience the run mode only and move, in the absence of collisions, i.e., sparse suspensions, in straight trajectories. Both strains swim at similar speeds; $13 \pm 2.2\,\mu$m/s for the WT during the run state and $11.2 \pm 1.8\,\mu$m/s for smooth-swimmers.

The two strains look alike under the microscope, with similar typical cell dimensions of $\sim 1 \times 3\,\mu$m in LB broth medium. All bacteria were stored at $-80\,^{\circ}$C in 50% glycerol stocks (kanamycin 100 μg/ml was added to frozen stocks of the Sm1420), selected on an LB plate (with the appropriate antibiotic), and grown overnight in LB broth at 30 °C and shaking (200 rpm) without antibiotics.

A small (5-μl) drop of an overnight culture was placed on a glass slide. The drop was constrained by a superhydrophobic ring printed on glass [polytetrafluoroethylene (PTFE) printed slides 63429-04, Electron Microscopy Sciences, Hatfield, PA] in order to prevent wetting and spreading, which may affect the dynamics of the bacteria or cause drifting. To prevent both evaporation and the blowing of air on the sample, the drop was enclosed in a small chamber, the top of which comprised a thin glass cover slip, while the surrounding wall was a metallic ring attached to the glass with vacuum grease (the glass cover slip was not in contact with the drop). The WT cells were swimming toward the drop surface and remained there while moving, increasing cell density from minimal to maximal within 6 min (which is slightly different than reported in [12]). On the liquid-air surface, cells formed a monolayer and were swirling in dynamic whirls and jets. Bacteria from the smooth-swimming strain were also found to form a swirling monolayer with dynamic whirls and jets, but they increased surface density on the drop surface slower because they were not migrating chemotactically to the surface. Increasing the surface density of cells from minimal to maximal lasted 35 min during which external conditions such as temperature and oxygen availability remained constant.

B. Observations

An optical microscope (Zeiss Axio Imager Z2) equipped with a LD 60 × phase-contrast objective lens was used to follow the microscopic motion. The microscope was placed in a temperature and humidity-controlled environment. A digital camera (GX 1050, Allied Vision Technologies) captured the microscopic motion at a rate of 100 frames per second and a spatial resolution of 1024×1024 pixels. Movies were taken for 20-min periods, streamed directly to the hard drive, resulting in 120 000 images in a sequence. The fraction of area occupied by bacteria, ρ, was calculated by measuring the number of dark pixels (above a threshold) covering the frame, then dividing by the entire number of pixels (1024×1024). In Fig. 1(a), we show a top-view image of the upper surface of the drop, taken by the optical microscope. The nearly spherical dark objects are the bacteria. See [12] for additional details.

C. Flow analysis

Recorded movies were converted to a sequence of single-frame images. Following standard preprocessing for noise reduction, the optical flow between each set of two consecutive frames was obtained using the Horn-Schunck method and reduced to a 64×64 grid. See [12] for details. Figure 1(b) shows an example of the velocity field calculated using the optical flow analysis for the cells shown in Fig. 1(a). Thus, the velocity field represents a coarse-grained description of the collective (and averaged) velocity of many bacteria in an effective grid cell.

In addition, we also calculated the vorticity of the flow, defined as the z component of the curl of the flow. The spatial correlation function of a vector field $\boldsymbol{\psi}(\boldsymbol{x}, t) \in \mathbb{R}^2$ is defined as

$$S(r) = Z^{-1}[\langle \boldsymbol{\psi}(\boldsymbol{x}, t) \cdot \boldsymbol{\psi}(\boldsymbol{y}, t) \rangle_{|\boldsymbol{x}-\boldsymbol{y}|=r,t} - \langle \boldsymbol{\psi}(\boldsymbol{x}, t) \rangle_{|\boldsymbol{x}-\boldsymbol{y}|=r,t} \cdot \langle \boldsymbol{\psi}(\boldsymbol{y}, t) \rangle_{|\boldsymbol{x}-\boldsymbol{y}|=r,t}],$$

where Z is a normalization constant such that $S(0) = 1$ and $\langle \cdots \rangle_{|\boldsymbol{x}-\boldsymbol{y}|=r,t}$ denotes averaging over all pairs of grid points $\boldsymbol{x}$ and $\boldsymbol{y}$ separated by distance r and over all frames with concentration in a given range. The temporal correlation function is taken as

$$T(t) = W^{-1}[\langle \boldsymbol{\psi}(\boldsymbol{x}, s) \cdot \boldsymbol{\psi}(\boldsymbol{x}, s+t) \rangle_{\boldsymbol{x},s}\} - \langle \boldsymbol{\psi}(\boldsymbol{x}, s) \rangle_{\boldsymbol{x},s} \cdot \langle \boldsymbol{\psi}(\boldsymbol{x}, s+t) \rangle_{\boldsymbol{x},s}],$$

where W is a normalization constant such that $T(0) = 1$ and $\langle \cdots \rangle_{\boldsymbol{x},t}$ denotes averaging over all grid points $\boldsymbol{x}$ and times $\boldsymbol{t}$.

D. Agent-based model

In order to investigate the experimental observations, we introduce a simplified model derived from the balance of forces and torques on each cell. Several agent-based approaches have been suggested, including dumbbells [41], regularized Stokeslets, [68] and dipoles [14,35,38]. The model introduced here adopts the dipole form and has been successfully used to study the different swimming behaviors of both motile and immotile cells. See Fig. 1(c) for a snapshot from a simulation. One of the main advantages of the model is that it is relatively simple to simulate. This is mostly due to the fact that the fluid equation for a point dipole has an analytical solution.

In comparison to real swimming bacteria, the streamlines generated by the model [depicted in Fig. 1(d)] in the intermediate to far field are qualitatively similar, but the approximation breaks down at the cell surface [69]. To make up for this inconsistency, a short-range repulsive potential in the form of a truncated Lennard-Jones potential is employed. The repulsive force also acts as an effective excluded-volume interaction. While other repulsive forces have been suggested

(e.g., Yukawa is used in [69]), the truncated Lennard-Jones potential has been used reliably in the past.

We consider N point particles (bacteria) $i = 1, \ldots, N$, with location $\boldsymbol{x}_i$ and orientation $\boldsymbol{d}_i$, a unit vector. We assume that bacteria move in a thin film and use the fluid velocity derived from two oppositely oriented force monopoles in a thin film, satisfying the Stokes equation [63]. The main difference between this thin film solution and the free-space solution is that the former decays as the cube of the distance while the latter decays only as the square of the distance. The faster decay results from the thin layer confinement on the flow. The only assumption required to use the thin film solution is that the film thickness is much smaller than the other relevant length scales [63].

To be precise, the fluid velocity at position $\boldsymbol{x} \in \mathbb{R}^2$ and time t, $\boldsymbol{u}(\boldsymbol{x}, t)$, is given by

$$\boldsymbol{u}(\boldsymbol{x}, t) = -\frac{l_1}{3\pi} \sum_{\{i=1\}}^{N} \{\nabla^3[\log(|\boldsymbol{x} - \boldsymbol{x}_i|)] \cdot \boldsymbol{d}_i(t)\} p_i \, \boldsymbol{d}_i(t), \tag{1}$$

where p_i is the size of the cell dipole moment (positive for pushers and negative for pullers) and l_1 is the film thickness. Noting that bacterial swimming results in a low Reynolds number flow, the cell dynamics are overdamped. Thus, considering the balance of forces and torques on each cell, we have

$$\dot{\boldsymbol{x}}_i = v_0 \boldsymbol{d}_i + \boldsymbol{u}(\boldsymbol{x}_i, t) + \varphi \sum_{\{i \neq j\}} \boldsymbol{F}(\boldsymbol{x}_i - \boldsymbol{x}_j), \tag{2}$$

$$\dot{\boldsymbol{d}}_i = -\boldsymbol{d}_i \times \left[\nabla \times \boldsymbol{u} + \frac{B}{2} \boldsymbol{d}_i \times (\nabla \boldsymbol{u} + \nabla^T \boldsymbol{u}) \boldsymbol{d}_i \right]. \tag{3}$$

The first term in (2) represents self-propulsion of each bacterium in the direction it is oriented with (isolated) swimming speed v_0. In general, this can be prescribed for each cell or may be time dependent, but in simulations it is taken as constant. The second term is the advection of the bacterium by the local flow generated by all the surrounding cells. The third term in (2) is a short-range soft repulsion between cells. For simplicity, we use a truncated (purely repulsive) Lennard-Jones-type potential that repels all cells within one cell length, l, and φ represents the strength of this interaction. The only difference between the smooth-swimmers and WT is that the WT tumbles on average once every τ s. The time between tumbles is modeled as an inhomogeneous Poisson process. When a cell is picked to tumble, a small rotational diffusion is added which is selected from a von Mises distribution with zero mean μ and standard deviation σ.

The equation for the orientation $\boldsymbol{d}_i$ was first introduced by Jeffery in 1922 [70] and allows the point dipoles to interact with the fluid as if they were prolate ellipsoids with aspect ratio λ. This shape is contained in the Bretherton constant $B = (\lambda^2 - 1)/(\lambda^2 + 1)$, which is between 0 (sphere) and 1 (pin). The first term in (3) represents the contribution to the orientation change due to the local vorticity while the second term in (3) represents rotation due to the local shear.

The system size used in the simulation is $L = 100l$, representing 100 particle lengths in each dimension, and an effective surface fraction $\rho = N\pi l^2/4L^2$ for N (up to 10 000 in simulations) was chosen to match experimental densities. Simulations were performed in a square computational domain with periodic boundary conditions. The dipole moment $p_i = F_p l = \zeta \eta l^2 v_0$ derived from the Stokes drag law relates the propulsion force F_p to the isolated swimming speed through the viscosity of the fluid η and a shape coefficient ζ. Simulations parameters are $\zeta\eta = 1$, $\tau = 2$ s, and $\sigma = \pi/12$. The cell aspect ratio is taken as 2:1, resulting in $B = 0.6$; swimming speed $v_0 = 10\,\mu$m/s; $\varphi = 0.001$; and $l = l_1 = 2\,\mu$m.

E. Continuum theory

Large collections of active moving particles are often modeled with continuum fields for the velocity and order parameter. In the last decade, several continuum theories have been proposed to investigate the collective dynamics of active moving particles [71].

Recently, a continuum model was derived by Heidenreich *et al.* [64,65] from a simple swimmer model first introduced by Saintillan and Shelley [71]. The derivation of the field equations allows us to link properties of the individual swimmers, such as the aspect ratio and propulsion speed, to the coefficients of the field theory describing collective dynamics. The swimmer model proposed in [71] is similar to the agent-based model introduced in the previous chapter. Using the same notation as Eqs. (2) and (3), the continuum model was derived from the overdamped Langevin equation:

$$\dot{\boldsymbol{x}}_i = v_0 \boldsymbol{d}_i + \boldsymbol{u}(\boldsymbol{x}_i, t) + \sqrt{2D} \; \boldsymbol{\eta}_x(t), \tag{4}$$

$$\dot{\boldsymbol{d}}_i = -\boldsymbol{d}_i \times \left[\nabla \times \boldsymbol{u} + \frac{B}{2} \boldsymbol{d}_i \times (\nabla \boldsymbol{u} + \nabla^T \boldsymbol{u}) \boldsymbol{d}_i \right] + \sum_{\{i \neq j\}} \boldsymbol{\Phi}(\boldsymbol{d}_i, \boldsymbol{d}_j) + \frac{1}{\sqrt{\tau}} \boldsymbol{\eta}_d(t). \tag{5}$$

Here, $\boldsymbol{\eta}_x$ and $\boldsymbol{\eta}_d$ denote Gaussian white noise modeling translational and rotational diffusion. The hydrodynamic flow $\boldsymbol{u}$ is given by the Stokes equation including an active stress of microswimmers. The term involving $\boldsymbol{\Phi}$ is a potential that describes the alignment interaction of the microswimmer (for details, see [65]). The additional term $\sum_{\{i \neq j\}} \boldsymbol{F}(\boldsymbol{x}_i - \boldsymbol{x}_j)$ which appears in (2) describes short-range soft repulsion. Including such a term in the overdamped Langevin equation, Eq. (4), is possible, but the derivation of continuum models becomes challenging due to the anisotropy of the force.

The continuum model without repulsion forces has been considered in previous studies and shows an excellent agreement with many aspects of the collective dynamical behavior of *Bacillus subtilis* in quasi-2D and -3D domains in a detailed comparison with experiments [5,39,65].

The continuum model consists of a polarization field $\boldsymbol{P}(\boldsymbol{x}, t)$, and a hydrodynamic flow field $\boldsymbol{u}(\boldsymbol{x}, t)$. See Figs. 1(e) and 1(f) for a snapshot from a simulation. We assume that the density ρ is constant and the incompressibility of $\boldsymbol{u}$ yields a divergence free field $\boldsymbol{P}$. The relaxation equation for the polar

order parameter is then given by

$$\dot{\boldsymbol{P}} = -\boldsymbol{u}\cdot\nabla\,\boldsymbol{P} + \boldsymbol{\Omega}\cdot\boldsymbol{P} + \kappa\,\boldsymbol{\Sigma}\cdot\boldsymbol{P} - \lambda_0\,\boldsymbol{P}\cdot\nabla\,\boldsymbol{P} - \alpha\,\boldsymbol{P} - \beta\,|\boldsymbol{P}|^2\,\boldsymbol{P} + \Gamma_2\nabla^2\boldsymbol{P} + \Gamma_4\nabla^4\boldsymbol{P} - p^*, \quad (6)$$

and the Stokes equation for the hydrodynamic flow reads

$$\nabla^2\boldsymbol{u} = c_{\mathrm{F}}\left(6\,c_{\mathrm{I}}\,\boldsymbol{P}\cdot\nabla\boldsymbol{P} + \nabla^2\boldsymbol{P} + \frac{1}{28}\nabla^4\boldsymbol{P}\right) + \nabla p_{\mathrm{eff}}, \quad (7)$$

where $\boldsymbol{\Omega}$ and $\boldsymbol{\Sigma}$ are the asymmetric and the symmetric part of the tensor $\nabla\boldsymbol{u}$. The first three terms of Eq. (6) describe advection, rotation, and stretching caused by the hydrodynamic flow gradients and the fourth term models self-advection. The next two terms involving α and β are the derivative of a Landau potential that models the isotropic-to-polar phase transition. The next two terms (with Γ_2 and Γ_4) describe hydrodynamic interactions and polar alignment. For sufficiently large self-propulsion speeds the parameter Γ_2 can take negative values which destabilizes the homogeneous state (polar or isotropic). The symbols p^* and p_{eff} are the hydrodynamic pressure and a Lagrange multiplier (to satisfy incompressibility).

The effective parameters $\Gamma_2, \Gamma_4, \kappa, \lambda_0, \alpha, \beta, c_{\mathrm{F}}, c_{\mathrm{I}}$ are linked to several physical quantities: the relaxation time of the rotational diffusion τ, the effective (kinematic) viscosity of the suspension μ_{eff}, the polar interaction range ε, the polar interaction strength γ_0, and several details of the microswimmers including the aspect ratio, length, self-propulsion speed, and the location of the hydrodynamic center (see below and [64,65] for details). In addition, some of these quantities, such as the viscosity, may also depend on the average density ρ. A detailed linear stability analysis reveals that the ratio Γ_4/Γ_2 is related to the fastest growing mode in the system [64]. This finite mode sets a typical length scale and typical vortex size, $\Lambda = 2\,\pi\sqrt{-2\Gamma_4\,/|\Gamma_2\,|}$.

The difference between the wild-type and smooth-swimmer strains can in principle be modeled by using different values of the relaxation time τ for the rotational diffusion. Large values of τ are related to large persistence lengths (relaxation time multiplied by the isolated swimming speed) of the swimmer (smooth-swimmer) where small values are related to small persistence lengths (WT). In principle, the smooth-swimmer can be modeled by using larger values of τ, around 20 s. However, the parameter involving the nonlinear term, $\boldsymbol{P}\cdot\nabla\,\boldsymbol{P}$, increases quadratically with the rotational relaxation time $\lambda_0 \propto \tau^2$ and large τ values lead to numerical instabilities. As a result, we only present results with $\tau = 1$ s, which is in accordance with realistic tumbling times of WT cells.

For numerical simulations, we use periodic boundary conditions and a pseudospectral code combined with an operator splitting technique for time integration [39]. The parameters follow from the microscopic properties of the swimmer, which we adapted to values realistic for wild-type cells of *S. marcescens*. The box length is $L = 50\,\mu$m and the length of the bacteria is $l = 2\,\mu$m. The area fraction is varied in the range $\rho = 0.3$–0.9 to match experimental densities. A cell aspect ratio of 2:1 and a self-propulsion velocity $v_0 = 20\,\mu$m/s is chosen. The range of polar interaction is assumed to be $\varepsilon = 3\,\mu$m. The strength of the polar alignment interaction is assumed to be $\gamma_0 = 0.004\ 1/\mu$m. This particular choice of microscopic parameter fixes the coefficients of (6) and (7) according to [65] as

$$\Gamma_2 = \frac{1}{10}\left(\frac{\varepsilon}{l}\right)^2\frac{c_{\mathrm{I}}}{P_r} - \frac{B}{15}\,P_r c_{\mathrm{F}}, \quad \Gamma_4 = -\frac{B}{420}\,c_{\mathrm{F}}P_r, \quad (8)$$

$$\lambda_0 = \frac{3}{5}c_{\mathrm{I}}\left(1 + \frac{2}{3}Bc_{\mathrm{F}}P_r\right), \quad \kappa = \frac{3}{5}B\left(1 - \frac{c_I}{3}\right), \quad (9)$$

$$\alpha = \frac{1 - c_{\mathrm{I}}}{P_r}, \quad \beta = \frac{3}{5}{c_{\mathrm{I}}}^2/P_r, \quad (10)$$

where $P_r = v_0\,\tau/l$ is the persistence number (persistence length $v_0\,\tau$ scaled by the microswimmer length l) and B is the shape parameter (Bretherton constant). The dimensionless parameter c_{I} denotes the strength of the polar interaction compared to the rotational diffusion time scale τ, i.e.,

$$c_{\mathrm{I}} = \frac{8\,\pi}{9}\frac{\varepsilon^3}{V_0}\gamma_0\,v_0\,\rho\tau, \quad (11)$$

and the second dimensionless parameter c_{F} characterizes the strength of the flow's response to the activity,

$$c_{\mathrm{F}} = \frac{2\pi}{10}\,\frac{\mu_0}{\mu_{\mathrm{eff}}}\frac{l^3}{V_0}\rho, \quad (12)$$

where V_0 is the volume of one bacterium and μ_0 is the viscosity of the surrounding fluid (see below and [65] for details).

III. RESULTS

The velocity and vorticity fields were measured experimentally for a range of surface densities ρ, from $\sim$0.2 to $\sim$0.85 [Figs. 2(a) and 2(b)]. In both the WT and the smooth-swimmers, the average speed and absolute vorticity were found to grow with increasing cell density reaching a maximum at about $\rho = 0.67$. This trend, in which speed increases with density, is the hallmark of collective bacterial swimming. At higher densities both measures decrease, possibly due to a jammed state. The two strains behaved similarly with a small difference in the value of the maximal absolute vorticity [Fig. 2(b)]. We have then looked at the distribution of velocities and vorticities by plotting the scaled fourth moment (kurtosis). The distribution of velocities and vorticities of the two strains was qualitatively different. Wild-type cells exhibited a normal distribution for all cell densities (kurtosis = 3). In contrast, smooth-swimmers had a normal distribution only at high densities and shifted from normal toward an exponential one (kurtosis = 6) for smaller densities [Figs. 3(a) and 3(b)].

Next, we looked at the spatiotemporal correlations of the moving cells [Figs. 4(a) and 4(b)]. See the Materials and Methods section for the precise definition. The correlation length and the correlation time of both the velocity and vorticity fields were calculated for the two strains at all cell densities, in each case by taking the value (on the x axis) at $1/e$ of the correlation. The results indicate no significant difference between the strains with fairly constant values of characteristic length and time scales along a large part of the measured densities (except for an abrupt increase for the velocity field at large densities).

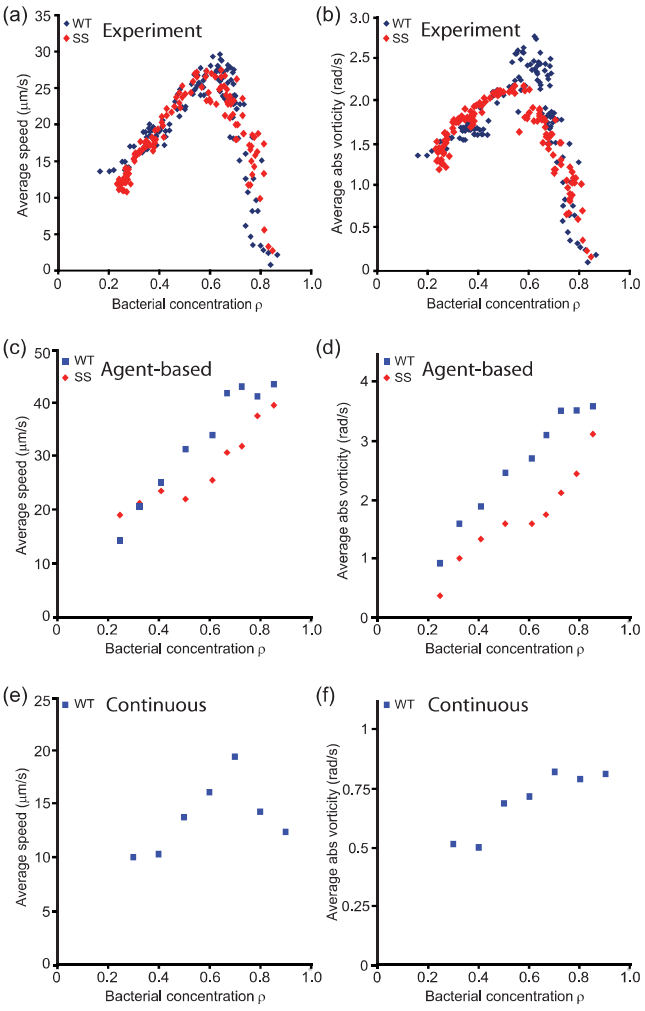

FIG. 2. Movement statistics. The mean average speed (a), (c), (e) and mean absolute vorticity (b), (d), (f) as a function of density obtained in experiments (a), (b), agent-based model middle (c), (d), and continuous model (e), (f). Both models capture the collective effect in which at low to medium concentrations, the mean speed increases with concentration. However, they fail to reproduce, or understimate, the jammed state observed experimentally at very high densities.

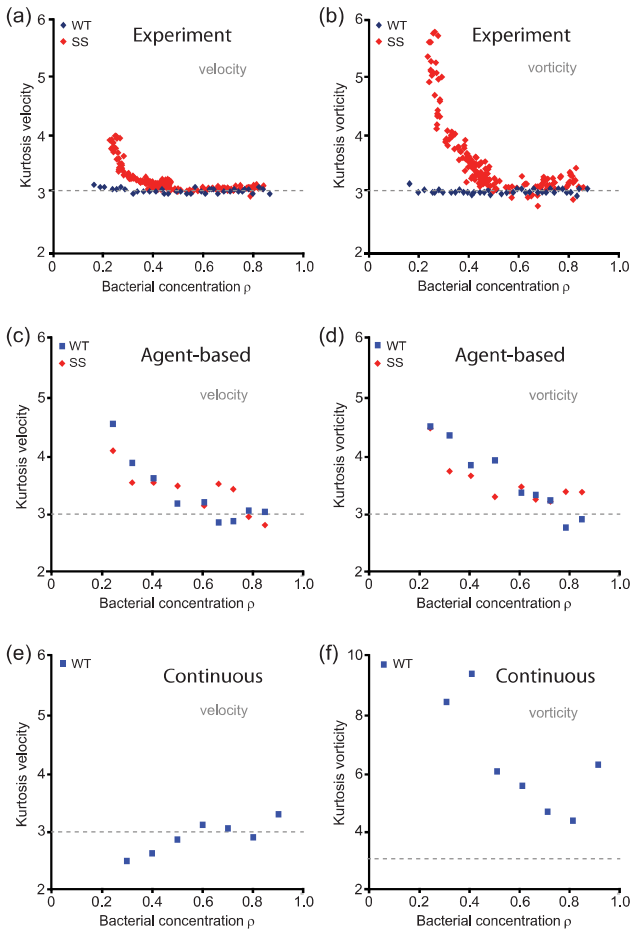

FIG. 3. Analysis of fluctuations. Experiments (a), (b) show that the velocity and vorticity distributions of WT cells are always Gaussian. However, smooth-swimmers show non-Gaussian statistics at low concentrations. In agent-based simulations (c), (d), both strains transition from non-Gaussian statistics at low concentrations to Gaussian at high densities. The continuous model (e), (f) shows Gaussian statistics of velocities for all concentrations. The kurtosis of the vorticity is noisy and high fluctuating.

The most surprising difference between the WT and the smooth-swimmers in experiments was found in the correlation between the local (linear) speed and the vorticity (rotational speed). Figure 5(a) shows that for WT cells, velocity and vorticity are uncorrelated; i.e., the speed of the cells does not depend on how fast the cells are rotating. However, in the smooth-swimmers, higher speeds are obtained for cells with larger vorticities and vice versa. In addition, this correlation is higher at low cell densities compared to crowded states. These results demonstrate that the collective dynamics of short elongated bacteria differ between WT and smooth-swimmers, in particular at low cell densities where direct short-range cell-cell interactions are weaker.

In order to gain insight on the mechanisms underlying the collective dynamics of the bacteria, the experimental results were compared with simulations. We begin with the discrete, agent-based model detailed in Sec. II D. In this model, each bacterium is represented as an individual point dipole that swims and interacts with the fluid flow generated by all other cells. The average (2D) area fraction, $\rho = N\pi l^2/4L^2$ was varied as in the experiments from ∼0.2 to ∼0.85 [Figs. 2(c) and 2(d)]. We find that in both the WT and the smooth-swimmers, the average speed and absolute value of the vorticity grow with the density; however, unlike the experiment, they continue to increase even at larger values. This is mainly due to the fact that at large densities the suspension in the experiments enters a jamming regime where excluded-volume effects dominate. Our model approximates hard-core steric interaction as a soft potential. As a result, it is expected that this description will become inaccurate at very high densities since the soft repulsion allows some overlap between the cells. Otherwise, the two strains behaved similarly in magnitude and qualitatively in behavior.

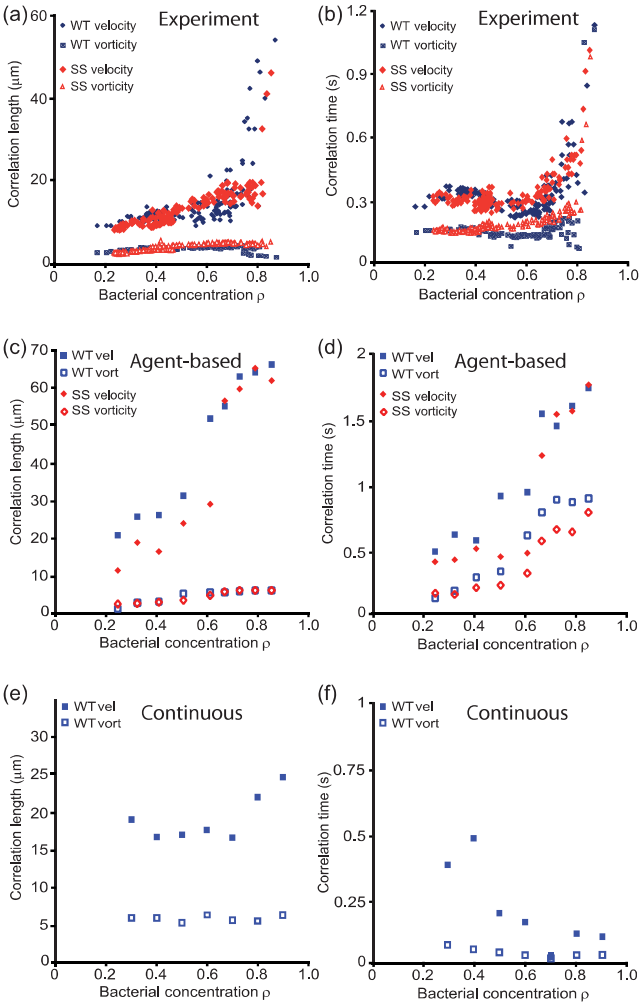

FIG. 4. Correlation length (a), (c), (e) and time (b), (d), (f) scales in experiments (a), (b), agent-based model (c), (d), and continuous (e), (f) simulations.

Next, as in the experiment, we looked at the shape of the probability distributions of velocities and vorticities by examining the kurtosis of each distribution [Figs. 3(c) and 3(d)]. At high densities, the kurtosis of both strains approaches 3 (normal distribution) and deviates from normal at lower densities. Moreover, we consider the spatiotemporal correlations generated by the flow [Figs. 4(c) and 4(d)]. As expected, the simulated correlation length and time increase as a function of density, and both strains show qualitatively similar behavior also matching the experimental observation.

The most notable difference between the experiment and agent-based simulations was found in the correlation coefficient between the local flow speed and the absolute vorticity [Fig. 5(b)]. In the model, the correlation coefficient decreases with density, but the two strains show qualitatively no difference. This differs from the experiment [Fig. 5(a)] where the WT shows no correlation. In addition, the magnitude of the correlation coefficient is larger in the agent-based simulations.

In order to gain insight into the physical origins of the jammed phase, which the agent-based model described above did not reproduce, we study a small variation. We hypothesize that jamming is due to some inelasticity which is significant when two cells become very close so they collide (inelastically), or their flagella overlap, creating friction. To this end, we incorporated an interaction that models some loss in velocity to two particles closer than a distance l, the cell size. At a distance $r < l$, cells experience a drag with rate $(l - r)/l$. In other words, we add an additional force, $(l - r)\boldsymbol{v}_i/l$.

At high concentrations, the cells are forced to be closer together. As a result, energy loss due to friction becomes significant and the overall speed decreases, as depicted in Fig. 6. We note that with the current parameters, the velocity decrease occurs at a higher concentration than observed in experiments; in addition the decrease is not as sharp. Nonetheless, our results indicate that the jammed phase may indeed be due to friction or other inelastic interactions at very short cell-cell distances.

Finally, we consider simulation results obtained with the continuum model described in Sec. II E. We find that the average speed and the absolute vorticity increase with increasing bacterial concentration similarly to the experiment ($\rho < 0.6$) and the agent-based model [Figs. 2(e) and 2(f)]. However, both speed and vorticity are too small by a factor of about 2. The monotonic increase of the collective velocity is related to the parameters of the Landau potential; i.e., $v_{\mathrm{coll}} = v_0\sqrt{-\alpha(\rho)/\beta(\rho)}$. Furthermore, our simulations show a decrease in speeds at high densities, although not as sharp as in experiments.

The values of the kurtosis in the velocity distribution [Fig. 3(e)] were independent of the density and approximately equal to 3, which is in accordance with the experimental WT results. However, the kurtosis of the vorticity [Fig. 3(f)] is highly noisy and does not seem reliable. The correlation length and time [Figs. 4(e) and 4(f)] are qualitatively in agreement with experiments and are of the same order of magnitude. There is some deviation at low densities, which is expected for a coarse-grained model. The difference can be explained by advection. In the continuum model, the correlation time depends on the advection, which increases with increasing bacterial concentration and in turn the correlation time decreases. Finally, we study the correlation between the local speed and the absolute value of the local vorticity. Here we found small correlations with a slight increase with density.

IV. DISCUSSION

We have studied the dynamics of collectively swimming bacteria, moving in a monolayer on a liquid-air surface. Our analysis shows that the contribution of flagellar tumbling to the collective motion changes across a range of bacterial concentrations.

In the experiment we have shown that short rods (aspect ratio ~1.5–2) of *S. marcescens* bacteria grown in broth will form a monolayer of collective flow with whirls and jets that occupy the upper surface of the liquid. While the dynamics of WT and smooth-swimming cells are similar at high cell density, it differs at low densities. This indicates that tumbling plays a role in the collective dynamics. For instance, Figs. 3(a) and 3(b) show that the distribution of velocities and vorticities depends on whether the cells are able to tumble, and the kurtosis deviates from normal values at

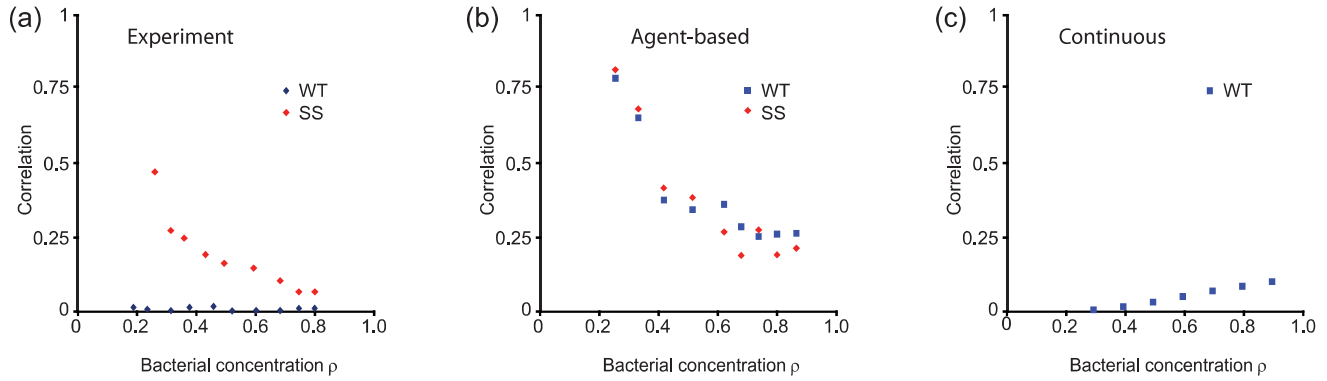

FIG. 5. Correlations between velocity and vorticity. Experiments (a) show that at low concentrations, the local speed of smooth-swimmers is correlated with the local absolute vorticity. The correlation decreases with increasing concentrations. In contrast, speed and vorticity of WT cells are not correlated at all concentrations. This suggests that the structure of the flow is different between WT and smooth-swimming cells. In agent-based simulations (b), both strains are qualitatively similar to real smooth-swimmers. In continuous simulations (c), correlations are small, as in WT, but are increasing with density.

densities around $\rho = 0.35$, fairly above the critical density for collective motion ($\rho = 0.25$). In addition, Fig. 5 shows that tumbling qualitatively changes the structure of the flow, as the correlation between the local speeds and vorticities depends on the ability to tumble, with obvious differences at even much higher densities such as $\rho = 0.6$. These results are consistent with experiments using swarming *B. subtilis* that are more elongated and form multilayer colonies [21].

In order to test whether the experimental results can be explained by known cell-cell interactions, two modeling approaches were considered.

As explained above, the approximation of the hydrodynamic cell-cell interaction as a Stokes dipole is expected to fail at high densities. Thus, the failure of the agent-based model to reproduce the jammed phase is consistent with the model assumptions. The modified model with inelastic short-range interactions suggests that dissipative effects such as inelastic collisions or friction play a significant role at such high densities. However, more work is required in order to understand the precise role of these effects. At lower densities, it is surprising that the differences between the WT and smooth-swimming strains cannot be accounted for by the inclusion of tumbling as random reorientation events at exponentially distributed times. The quantitative differences between the experimental and modeled dynamics, across all measured densities, suggest that tumbling has a more fundamental role in the bacterial dynamics than merely increasing rotational diffusion.

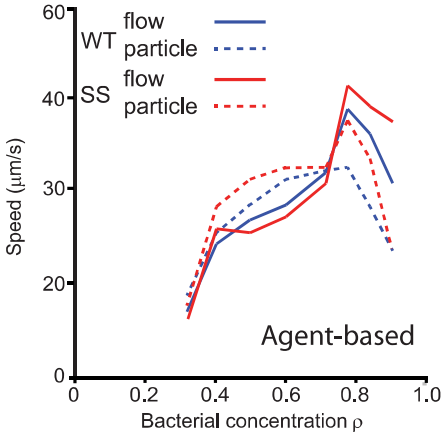

FIG. 6. The average speed of the flow (full line) and particles (dashed line) in the modified agent-based model with inelastic short-range friction. At high concentrations, the cells are forced to be closer together and energy loss due to friction becomes significant. As a result, the overall speed decreases, in qualitative agreement with the jammed phased observed in experiments. Blue: WT; red: smooth-swimmers.

The continuum model has two assumptions that yield to simplifications which are mainly responsible for deviations from experiments: first, that the self-propulsion velocity of all bacteria is constant (in time), and second, that the density is constant (both in time and space). Moreover, modeling smooth-swimmers by adapting the rotational diffusion is probably too simple and neglects the discrete nature of tumbling events. Even though such assumptions are typical for continuous, coarse-grained models, we have shown here that they can have a significant impact on the dynamics.

Overall, our results indicate that modeling the collective dynamics of two-dimensional swimming bacteria is a complex task where the theory often fails to describe the full range of the dynamics across densities. Moreover, we find that our agent-based model may be more valid for the modeling of smooth-swimmers, while the continuous model gives reasonable results for WT cells in which the fluctuations of viscosities is Gaussian and uncorrelated with the local vorticity.

The results presented here compare only two bacterial strains from the same species and two models. However, the physical view of bacteria as self-propelled particles or natural examples of active matter suggest such systems share some universal properties. As a result, it is expected that other bacterial species that exhibit collective dynamics will behave similarly. Our experimental results represent a useful basis for checking other two-dimensional models for collective motion of swimmers including self-propelled rods [61,72–76],

models with complex alignment interactions [77], or other more realistic models with detailed cell-cell interactions [78].

ACKNOWLEDGMENTS

We thank Rasika M. Harshey and Jonathan D. Partridge for sending the strains. G.A. and A.B. are thankful for partial support from The Israel Science Foundation's Grant No. 373/16. G.A., S.H., M.B., and A.B. are thankful for partial support from The Deutsche Forschungsgemeinschaft (The German Research Foundation DFG) Grants No. HE5995/3-1 and No. BA1222/7-1. S.D.R. is thankful for internal support from the Cleveland State University Office of Research.

[1] L. Turner, W. S. Ryu, and H. C. Berg, J. Bac. **182**, 2793 (2000).
[2] H. C. Berg, *E. coli in Motion* (Springer Science & Business Media, New York, 2004).
[3] B. Ilkanaiv, D. B. Kearns, G. Ariel, and A. Be'er, Phys. Rev. Lett. **118**, 158002 (2017).
[4] L. H. Cisneros, J. O. Kessler, S. Ganguly, and R. E. Goldstein, Phys. Rev. E **83**, 061907 (2011).
[5] H. H. Wensink, J. Dunkel, S. Heidenreich, K. Drescher, R. E. Goldstein, H. Löwen, and J. M. Yeomans, Proc. Natl. Acad. Sci. USA **109**, 14308 (2012).
[6] F. Peruani, A. Deutsch, and M. Bär, Phys. Rev. E **74**, 030904(R) (2006).
[7] S. Weitz, A. Deutsch, and F. Peruani, Phys. Rev. E **92**, 012322 (2015).
[8] F. Peruani, J. Starrus, V. Jakovljevic, L. Søgaard-Andersen, A. Deutsch, and M. Bär, Phys. Rev. Lett. **108**, 098102 (2012).
[9] J.-M. Swiecickia, O. Sliusarenko, and D. B. Weibel, Integr. Biol. **5**, 1490 (2013).
[10] A. Sokolov and I. S. Aranson, Phys. Rev. Lett. **103**, 148101 (2009).
[11] C. Blanch-Mercader and J. Casademunt, Soft Matter **13**, 6913 (2017).
[12] A. Rabani, G. Ariel, and A. Be'er, PLoS One **8**, e83760 (2013).
[13] I. S. Aranson, A. Sokolov, J. O. Kessler, and R. E. Goldstein, Phys. Rev. E **75**, 040901(R) (2007).
[14] S. D. Ryan, B. M. Haines, L. Berlyand, F. Ziebert, and I. S. Aranson, Phys. Rev. E **83**, 050904(R) (2011).
[15] C. W. Wolgemuth, Biophys. J. **95**, 1564 (2008).
[16] J. Dunkel, S. Heidenreich, M. Bär, and R. E. Goldstein, New J. Phys. **15**, 045016 (2013).
[17] R. Grossmann, P. Romanczuk, M. Bär, and L. Schimansky-Geier, Phys. Rev. Lett. **113**, 258104 (2014).
[18] V. Bratanov, F. Jenko, and E. Frey, Proc. Natl. Acad. Sci. USA **112**, 15048 (2015).
[19] M. James and M. Wilczek, Eur. Phys. J. E **41**, 21 (2018).
[20] D. Nishiguchi and M. Sano, Phys. Rev. E **92**, 052309 (2015).
[21] M. Sidortsov, Y. Morgenstern, and A. Be'er, Phys. Rev. E **96**, 022407 (2017).
[22] A. Be'er and R. M. Harshey, Biophys. J. **101**, 1017 (2011).
[23] H. P. Zhang, A. Be'er, E.-L. Florin, and H. L. Swinney, Proc. Natl. Acad. Sci. USA **107**, 13626 (2010).
[24] A. Be'er, S. K. Strain, R. A. Hernández, E. Ben-Jacob, and E.-L. Florin, J. Bacteriol. **195**, 2709 (2013).
[25] X. Chen, X. Dong, A. Be'er, H. L. Swinney, and H. P. Zhang, Phys. Rev. Lett. **108**, 148101 (2012).
[26] X. Chen, X. Yang, M. Yang, and H. P. Zhang, Europhys. Lett. **111**, 54002 (2015).
[27] S. Benisty, E. Ben-Jacob, G. Ariel, and A. Be'er, Phys. Rev. Lett. **114**, 018105 (2015).
[28] M. T. Butler, Q. Wang, and R. M. Harshey, Proc. Natl. Acad. Sci. USA **107**, 3776 (2010).
[29] M. F. Copeland and D. B. Weibel, Soft Matter **5**, 1174 (2009).
[30] N. C. Darnton, L. Turner, S. Rojevsky, and H. C. Berg, Biophys. J. **98**, 2082 (2010).
[31] J. D. Partridge and R. M. Harshey, J. Bacteriol. **195**, 909 (2013).
[32] G. Ariel, A. Shklarsh, O. Kalisman, C. Ingham, and E. Ben-Jacob, New J. Phys. **15**, 125019 (2013).
[33] A. Be'er, R. S. Smith, H. P. Zhang, E.-L. Florin, S. M. Payne, and H. L. Swinney, J. Bacteriol. **191**, 5758 (2009).
[34] G. Ariel, A. Rabani, S. Benisty, J. D. Partridge, R. M. Harshey, and A. Be'er, Nat. Commun. **6**, 8396 (2015).
[35] S. D. Ryan, G. Ariel, and A. Be'er, Biophys. J. **111**, 247 (2016).
[36] D. Roth, A. Finkelshtein, C. Ingham, Y. Helman, A. Sirota-Madi, L. Brodsky, and E. Ben-Jacob, Environ. Microbiol. **15**, 2532 (2013).
[37] H. P. Zhang, A. Be'er, R. S. Smith, E.-L. Florin, and H. L. Swinney, EPL **87**, 48011 (2009).
[38] S. D. Ryan, A. Sokolov, L. Berlyand, and I. S. Aranson, New J. Phys. **15**, 105021 (2013).
[39] J. Dunkel, S. Heidenreich, K. Drescher, H. H. Wensink, M. Bär, and R. E. Goldstein, Phys. Rev. Lett. **110**, 228102 (2013).
[40] E. Lushi, H. Wioland, and R. E. Goldstein, Proc. Natl. Acad. Sci. USA **111**, 9733 (2014).
[41] J. P. Hernandez-Ortiz, P. T. Underhill, and M. D. Graham, J. Phys.: Condens. Matter **21**, 204107 (2009).
[42] L. Turner, R. Zhang, N. C. Darnton, and H. C. Berg, J. Bacteriol. **192**, 3259 (2010).
[43] S. Zhou, A. Sokolov, O. D. Lavrentovich, and I. S. Aranson, Proc. Natl. Acad. Sci. USA **111**, 1265 (2014).
[44] M. F. Copeland, S. T. Flickinger, H. H. Tuson, and D. B. Weibel, Appl. Environ. Microbiol. **76**, 1241 (2010).
[45] H. H. Tuson, M. F. Copeland, S. Carey, R. Sacotte, and D. B. Weibel, J. Bacteriol. **195**, 368 (2013).
[46] A. Sokolov and I. S. Aranson, Phys. Rev. Lett. **109**, 248109 (2012).
[47] A. Sokolov, I. S. Aranson, J. O. Kessler, and R. E. Goldstein, Phys. Rev. Lett. **98**, 158102 (2007).
[48] V. Gyrya, I. S. Aranson, L. V. Berlyand, and D. Karpeev, Bull. Math. Biol. **72**, 148 (2010).
[49] G. K. Nachiket and J. D. Shrout, PLoS One **6**, e20888 (2011).
[50] M. Burkhart, A. Toguchi, and R.M. Harshey, Proc. Natl. Acad. Sci. USA **95**, 2568 (1998).
[51] S. Mariconda, Q. Wang, and R. M. Harshey, Mol. Microbiol. **60**, 1590 (2006).
[52] Q. Wang, A. Suzuki, S. Mariconda, S. Porwollik, and R. M. Harshey, EMBO J. **24**, 2034 (2005).
[53] A. Toguchi, M. Siano, M. Burkart, and R. M. Harshey, J. Bacteriol. **182**, 6308 (2000).

[54] H. C. Berg, Curr. Biol. **15**, R599(R) (2005).
[55] R. M. Harshey and T. Matsuyama, Proc. Natl. Acad. Sci. USA **91**, 8631 (1994).
[56] S. D. Ryan, L. Berlyand, B. M. Haines, and D. Karpeev, Multiscale Model. Simul. **11**, 1176 (2013).
[57] D. B. Kearns and R. Losick, Mol. Microbiol. **49**, 581 (2004).
[58] A. Sokolov, L. D. Rubio, J. F. Brady, and I. S. Aranson, Nat. Commun. **9**, 1322 (2018).
[59] H. M. López, J. Gachelin, C. Douarche, H. Auradou, and E. Clément, Phys. Rev. Lett. **115**, 028301 (2015).
[60] Y. L. Chuang, T. Chou, and M. R. D'Orsogna, Phys. Rev. E **93**, 043112 (2016).
[61] Y. Yang, V. Marceau, and G. Gompper, Phys. Rev. E **82**, 031904 (2010).
[62] M. C. Marchetti, J. F. Joanny, S. Ramaswamy, T. B. Liverpool, J. Prost, M. Rao, and A. Simha, Rev. Mod. Phys. **85**, 1143 (2013).
[63] B. Cui, H. Diamant, B. Lin, and S. A. Rice, Phys. Rev. Lett. **92**, 258301 (2004).
[64] S. Heidenreich, J. Dunkel, S. H. L. Klapp, and M. Bär, Phys. Rev. E **94**, 020601(R) (2016).
[65] H. Reinken, S. H. L. Klapp, M. Bär, and S. Heidenreich, Phys. Rev. E **97**, 022613 (2018).
[66] A. Baskaran and M. C. Marchetti, Proc. Natl. Acad. Sci. USA **106**, 15567 (2009).
[67] K. Tunstrøm, Y. Katz, C. C. Ioannou, C. Huepe, M. J. Lutz, and I. D. Couzin, PLoS Comput. Biol. **9**, e1002915 (2013).
[68] R. Cortez, L. Fauci, and A. Medovikov, Phys. Fluids **17**, 031504 (2005).
[69] K. Drescher, J. Dunkel, L. H. Cisneros, S. Ganguly, and R. E. Goldstein, Proc. Natl. Acad. Sci. USA **108**, 10940 (2011).
[70] G. B. Jeffery, Proc. R. Soc. London, Ser. A **102**, 161 (1922).
[71] D. Saintillan and M. J. Shelley, C. R. Phys. **14**, 497 (2009).
[72] H. H. Wensink and H. Löwen, J. Phys.: Condens. Matter **24**, 464130 (2012).
[73] A. Kaiser and H. Löwen, Phys. Rev. E **87**, 032712 (2013).
[74] A. Kaiser, A. Sokolov, I. S. Aranson, and H. Löwen, IEEE Trans. NanoBiosci. **14**, 260 (2015).
[75] S. R. McCandlish, A. Baskaran, and M. F. Hagan, Soft Matter **8**, 2527 (2012).
[76] M. Abkenar, K. Marx, T. Auth, and G. Gompper, Phys. Rev. E **88**, 062314 (2013).
[77] R. Grossmann, P. Romanczuk, M. Bär, and L. Schimansky-Geier, Eur. Phys. J.: Spec. Top. **224**, 1325 (2015).
[78] A. Zöttl and H. Stark, Phys. Rev. Lett. **112**, 118101 (2014).